Geofísica Internacional (2024) **63-4**: 1175 - 1191

The Extraction and Structural Analysis of Lineaments Around Gülsehir (Nevşehir) Using GIS Methods

Ramazan Demircioğlua*[1], Yaşar Erenb[2] and Berkant Coşkunerb[2]

Abstract

This study aims to determine the lineaments in the Palaeozoic - Cenozoic rocks outcropping around Gülşehir (Nevşehir) using Landsat-8 satellite images, shaded relief and slope maps and to compare them with field studies. Faulted structures in the region are formed by E-W trending thrusts, NE-SW trending reverse faults and NW-SE trending normal faults. A Digital Elevation Model (DEM) was used to produce the lineament maps. Google Earth and Landsat 8 images were also used. The shaded relief map (SRM) and slope map were derived from the DEM. The analysis of the produced linearity maps showed that the slope map and the integrated (SRM) map were more consistent with the field data. The lineament maps derived from the slope maps are largely consistent with the faults and fractures identified in the field. According to the strike maps, N15-30^{0}E and N75-90^{0}W orientated structures dominate the region. Lineaments show a tendency in all directions due to polyphase deformation.

Key words: Turkey, Central Anatolia, Nevşehir, fault, fracture, lineament.

Resumen

El objetivo de este estudio es determinar los lineamientos de las rocas paleozoicas y cenozoicas que afloran en los alrededores de Gülşehir (Nevşehir) utilizando imágenes de satélite Landsat-8, mapas de relieve sombreado y de pendientes, y compararlos con estudios de campo. Las estructuras falladas de la región están formadas por empujes con tendencia E-O, fallas inversas con tendencia NE-SW y fallas normales con tendencia NW-SE. Para elaborar los mapas de lineamientos se utilizó un modelo digital de elevación (MDE). También se utilizaron imágenes de Google Earth y Landsat 8. El mapa de relieve sombreado (SRM) y el mapa de pendientes se obtuvieron a partir del MDE. El análisis de los mapas de linealidad producidos mostró que el mapa de pendientes y el mapa integrado (SRM) eran más coherentes con los datos de campo. Los mapas de lineación obtenidos a partir de los mapas de pendiente coinciden en gran medida con las fallas y fracturas identificadas en el campo. Según los mapas de rumbo, las estructuras orientadas N15-30^{0}E y N75-90^{0}W dominan la región. Los lineamentos muestran una tendencia en todas las direcciones debido a la deformación polifásica.

Palabras clave: Turquía, Anatolia Central, Nevşehir, falla, fractura, lineamento.

Received: June 29, 2023 ; March 27, 2024; Published on-line: October 1, 2024.

Editorial responsibility: Dr. Roberto Bonifaz Alfonzo

* Corresponding author: Ramazan Demircioğlu, ra.demircioglu@gmail.com
[1] Department of Emergency Aid and Disaster Management, Aksaray University, Aksaray, Turkey.
[2] Department of Geology Engineering, Konya Technical University, Konya, Turkey.

Ramazan Demircioğlua, Yaşar Erenb, Berkant Coşkunerb

https://doi.org/10.22201/igeof.2954436xe.2024.63.4.1725

1. Introduction

The study area is located around the north of Gülsehir (Nevşehir-Central Anatolia-Turkey) (Figure 1). There are many geological studies in this area (Seymen, 1981a, Demircioğlu, 2014, Atabey 1988, Dirik, Göncüoğlu, 1996, Koçyiğit 1984, Eren 2003, Koçyiğit 2003, Doğan *et al.*, 2010, Koçyiğit and Doğan 2016).

In this study, the tectonic lineaments of the linear structures in the area, such as faults and fractures, which were determined by field studies, were obtained using satellite and Google Earth images. The lineaments obtained from the field surveys and the images were compared. Although the origin and characteristics of the lineaments are different, the lineaments obtained by remote sensing methods are compared and evaluated with both the orientation data and the fieldwork data.

There is no previous remote sensing study in the study area. The detection of lineaments will be important for mineral exploration, and water and geothermal studies to be carried out in the area.

Gold prospecting has intensified in the study area in recent years. In particular, faults and fractures play an important role in these searches. This study is also important in this regard.

Recently, especially after the development of satellite technology in the 1960s and 1970s, satellite images and aerial photographs have been used extensively. The extraction of linear structures in the field makes important contributions to the study of water resources, oil and gas fields, and mineral deposits. Recently, developments in satellite, drone, and lidar technology have been used quite frequently to reveal the lineaments in an area, some of which are; Kresic (1995), Koike *et al.* (1995), Lee T.H., Moon W.M. (2002), Hung *et al.* (2005), Raharimahefa and Kusky, (2009), Begg and Mouslopoulou, (2010), Bruning *et al.* (2011), With and Carter, (2016). Tessema *et al.* (2012), Bhuiyan (2015), Raj *et al.* (2017), Altafi *et al.* (2017), Listyani vd. (2018), Takorabt *et al.* (2018), Keppel *et al.* (2020), Wannous *et al.*, (2021), El-Magd and Embaby (2021), Abdelouhed *et al.* (2022), Goswami *et al.* (2022), Vijhani *et al.* (2022), Şeyh *et al.* (2022), Abebrese *et al.* (2022) studies.

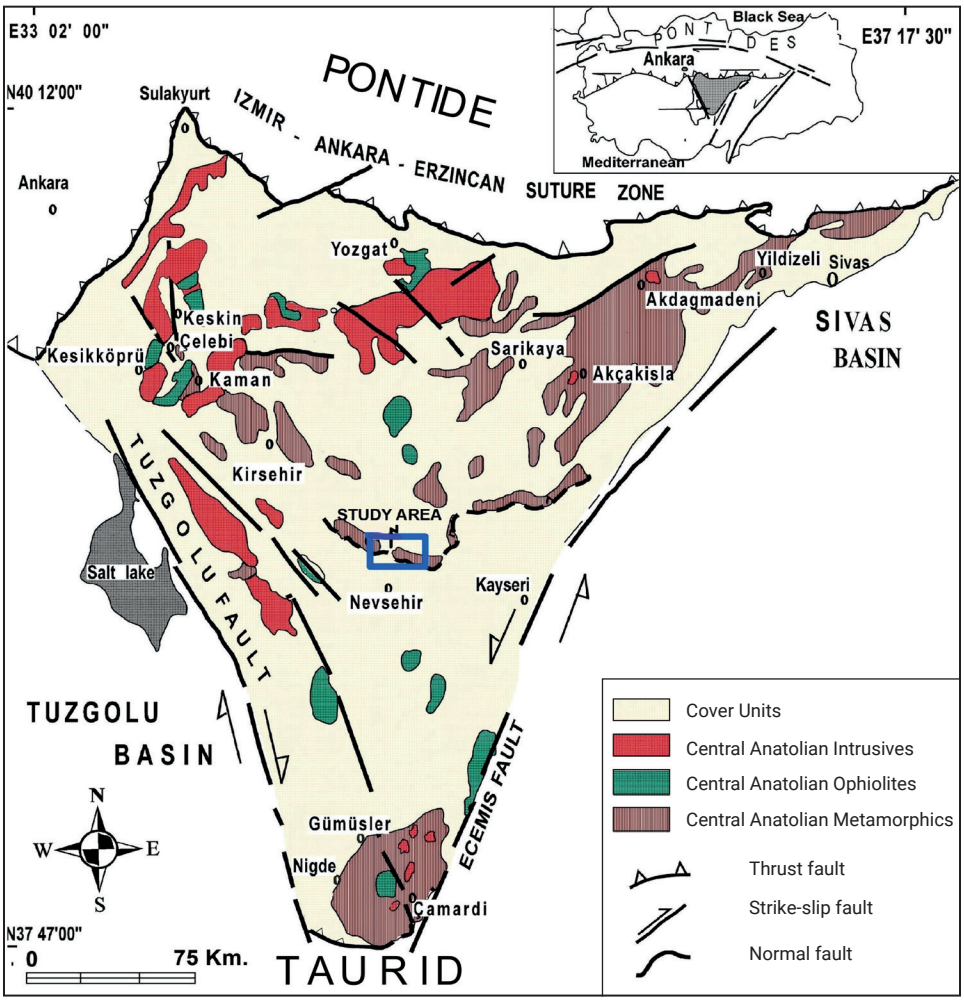

Figure 1. Spatial map of the study area and its surroundings (modified from Kuşçu, 2001).

Lineaments seen in aerial and satellite imagery or digital elevation modelling (B. E. Hobbs, Means, and Williams, 1976; W. H. Hobbs, 1904, Tagnon *et al.*, 2020, Hajaj *et al.*, 2022, Ahmadi *et al.*, 2023) can be natural or artificial (man-made). In this sense, lineaments can be of natural origins, such as a fault trace, a valley margin trace, a trace of a major fold or fault structure, a stream trace, and a ridge trace. There are important studies on this subject (Isiorho 1985; Drury and Walker, 1987; Cracknell and Heyes 1993; Jordan, G. and Schott, B., 2005). It may also be artificial, such as a motorway, dam crest, field boundary, or (man-made) watercourse. The determination of geological lineaments using Geographic Information System (GIS) or satellite imagery as well as field studies is economical (planning and construction of engineering structures such as oil, water, underground water and mineral exploration and dams, bridges, canals and tunnels) and important for determining some parts of natural disasters. With the development of GIS methods and satellite imagery (Jacques, Machado, and Nummer, 2012; Madani, 2001; Masoud and Koike, 2006; Sedrette and Rebaï, 2016; Suzen and Toprak, 1998), these methods are increasingly used for lineament determination (Cracknell and Heyes 1993, Abdullah *et al.*, 2010; Abdullah *et al.*, 2013; Ganguly and Mitran, 2016). In this study, shaded relief maps (hillshade, shaded relief maps), profile curvature and slope gradient maps derived from satellite imagery such as Landsat 8 (The natural colour composition was obtained using a combination of red (band 4), green (band 3) and blue (band 2)), Google Earth, and digital elevation model (DEM) maps of the study area were used. Automatic lineament maps of the Nevşehir, Gülşehir (Central Anatolia-Turkey) area using slope gradient maps, creation of these lineament maps using Arc-GIS (Esri, USA, 2020), Geomatica (PCI Geomatics, Canada, 2018), Rockwork (RockWare Inc., Golden, USA, 2019)) software, and faults and joints determined by field observations were compared.

2. Materials and Methods

In this study, Landsat ETM-8 satellite images (Landsat-8-OLI (Operational Land Imager) uses a band combination of natural colour composition, red (4), green (3) and blue (2)), and Google Earth images (from Digital Globe and CNES/Airbus) were used as satellite images for the production of automatic lineament maps. In addition, a Digital Elevation Model (DEM) was created using a Geographic Information System (GIS) for the production of automatic lineament maps. For the Digital Elevation Model, digitised topographic maps of the study area were used. In this study, lineaments were obtained from satellite images, Google Earth images and images obtained from the Arc-GIS program and compared with lineaments obtained from field studies. Compared to previous studies, different combination studies were carried out.

Satellite imagery captures objects' responses in different parts of the electromagnetic spectrum. Meanwhile, digital elevation models and their derivatives represent the terrain digitally, showing a range of features such as slopes, gradients, and fault scarps.

From the DEM map, shaded relief maps were prepared with different illumination directions (the height is related to the variation of the angle of the light source) and integrated shaded relief maps were prepared and processed from these maps. The slope gradient map and profile curvature map obtained from the DEM map were also used to create an automatic linement map. An edge sharpening filter was applied using the Line module to produce a lineament map from these images and maps. Although many different threshold values were given in the literature during the application, the threshold values suggested by Sedrette and Rebaï (2016) and given below were used in this study (Table 1).

Strike and strike length rose maps were created from the generated lineament maps.

Envi, Geomatica, and ArcGIS 10.0 were used to automatically generate lineament maps, and Rockworks software was used for the rose diagrams. The process of obtaining lineament from satellite and Google Earth images is given in Figure 2 as a flowchart.

3. Geological background

The research region's oldest units are the Palaeozoic-Mesozoic Kırşehir Massif, as well as the Kaman Group's Tamadag and Bozçaldag metamorphics. The Late Cretaceous Akçataş syenitoid and Kötüdag andesite intrude on these formations. These basement units cover the Late Paleocene-Middle Eocene Ayhan Group strata in an unconformable manner (Figure 3). The Saytepe, Esefin, Kubaca, Ilicek, Alıçlı, Lalelik, and Altıpınar formations are all part of the Ayhan Group. Conglomerate, sandstone, and mudstone strata make up the Saytepe Formation. These formations are transitional both laterally and vertically.

Table 1. Threshold values used for Arc-Gis analyses.

Filter Type: Edge Sharpening Filter
Threshold values:
RADI (Radius of filter in pixels)=10
GTHR (Threshold for edge gradient)=100
LTHR (Threshold curve length)=30
FTHR (Threshold for line fitting error)=3
ATHR (Threshold for angular difference)=30
DTHR (Threshold for linking distance) =20

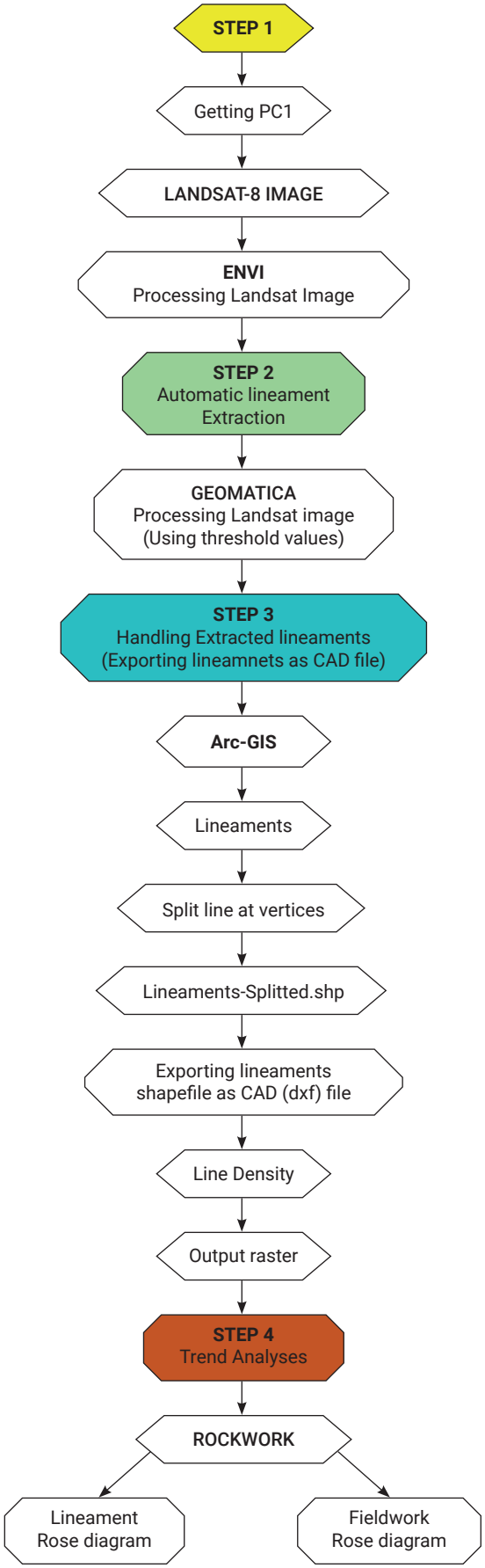

Figure 2. Flowchart for obtaining lineament and rose diagrams.

They were found in a variety of settings, from terrestrial to offshore shallow sea.

According to the algal and *Ataxophragmidae* units, Göncüoglu *et al.* (1993) judged it to be coeval with the top sections of the Eskiburç Formation in the southeast of the research region. Sandstone, siltstone, claystone, and limestone make up the Esefin Formation. They developed in a shallow sea environment. Sandstone, siltstone, shale, and limestone make up the Kubaca Formation. Based on the Late Palaeocene Saytepe Formation below and the Middle Eocene Lalelik Formation above, the stratigraphic connections are simply an early-middle Eocene date. The lithological properties and fossil richness of the units above and below, on the other hand, indicate that they are products of a marine environment.

Shale, sandstone, and siltstone make up the Ilicek Formation. There were no fossils detected in the thin sections of samples obtained from the unit's rocks. It is of Early-Middle Eocene age, as determined by the Early-Middle Eocene and Lutesian units below and above. The properties of the rock indicate that it was most likely created in a shallow marine-terrestrial environment. Sandstones, siltstones, mudstones, and limestones make up the Alıçlı Formation. Globigerina sp. fossils have been discovered amid the clay layers. This suggests that the unit was deposited in the open sea. Sandstone, siltstone, claystone, marl, and mudstone make up the Lalelik Formation. According to the method of nannofossil identification acquired from the marls, the age of the unit is Lower-Middle Eocene.

All of the preceding units are unconformably overlain by the Yaylacık group's Tuzköy and Yüksekli formations, which are products of the lacustrine environment. The Yaylacık Group is unconformably overlain by the Late Miocene-Pliocene Urgup Formation. The Avanos Group's Pliocene-Pleistocene Kızılrmak Formation, Güvercinlik Pebbles, and Gülşehir Basalt unconformably overlie the Urgüp Formation. The region's youngest units include Quaternary (Holocene) age Balkaya travertine, recent slope debris, and recent alluvium composed of stones, gravel, sand, silt, and clay (Figure 2).(Seymen, 1981, Atabey *et al.*, 1988, Göncüoğlu *et al.*, 1993, Demircioğlu, 2014).

3.1 Structural Geology

The rocks outcropping in the study area have been affected by tectonic movements in paleo-tectonic and neo-tectonic periods and have undergone polyphase deformation. Depending on the deformations, the rocks in the area have acquired poly-phase folding and faulted and fractured structures in different directions. A structural map of the study area was also prepared (Demircioğlu, 2014). In addition, the faults and fold axes observed in the area are shown on the structural geological map (Figure 4).

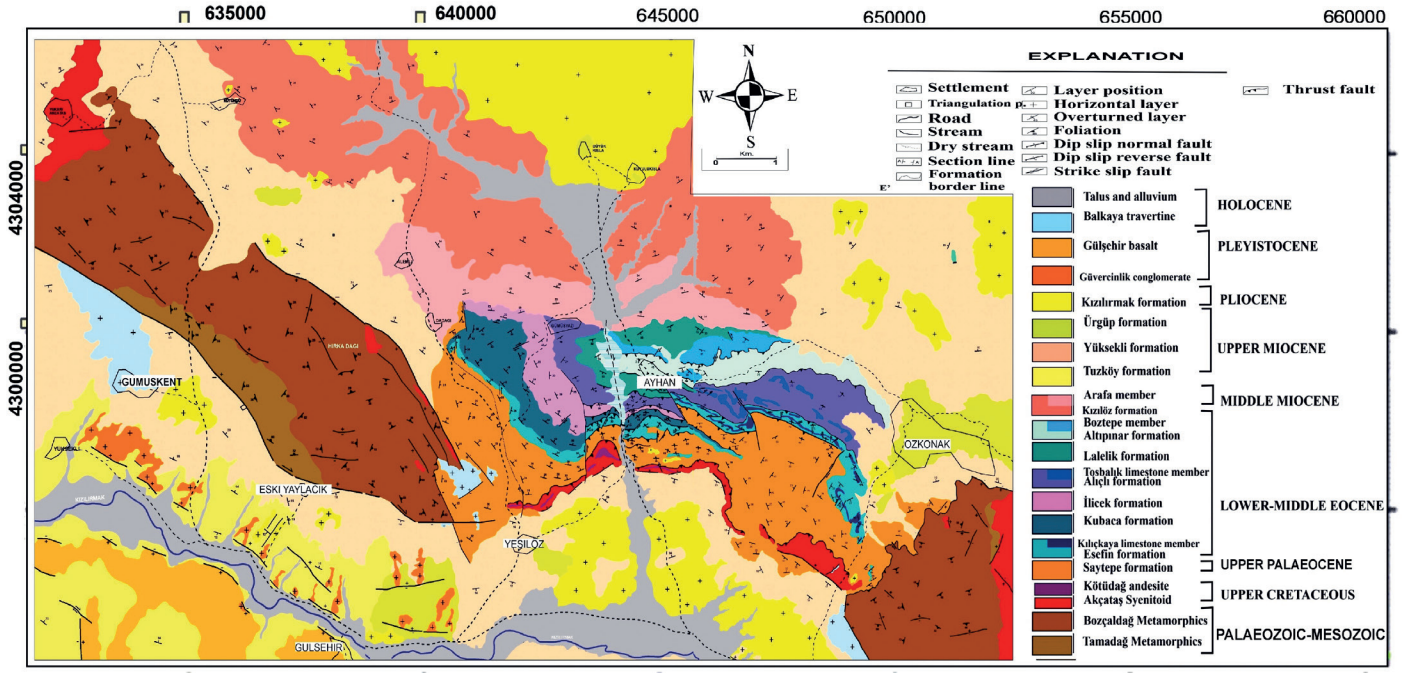

Figure 3. Geological map of the study area.

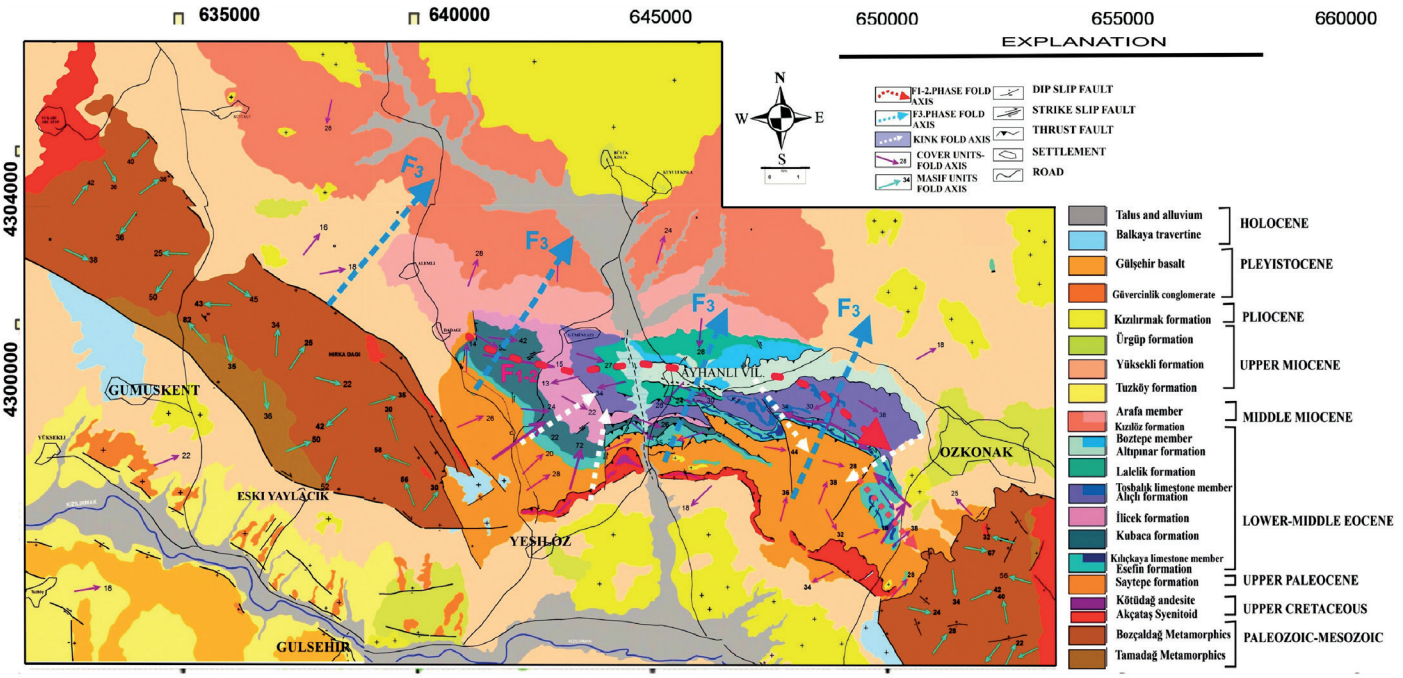

Figure 4. Geological map of the study area and faults (Demircioğlu *et al.*, 2018).

The Alpine events in the Cretaceous deformed the pre-Late Miocene rock assemblages in the study area due to the closure of the Neo-Tethys ocean, underwent polyphase folding and acquired thrust fault structures (Demircioğlu, 2014). In addition to these palaeo-tectonic events, the rocks in the study area have also been affected by the block faulting that developed during the Neo-Tethys. In the basins created by block faulting, rocks including terrestrial, lacustrine and volcanic rocks were deposited during the Late Miocene-Pliocene. Alluvial fans and alluvial deposits were widespread in the Plio-Quaternary basins. The normal faults that form the Miocene-Quaternary basins strike NNE-SSW and WNW-ESE.

4. Results

4.1 Automated lineament maps from Google Earth images

Initially, Google Earth Pro (**https://www.google.com/intl/tr/earth**) images were used to generate the automated lineament map of the study area (Figure 5).

The Google Earth image The Google Earth image representing the study area (1237 m. altitude and 1980x1020 pixel resolution) was downloaded from the internet and the linearity map of the image was created using the necessary filters and thresholds (Figure 5a, 5b). representing the study area was downloaded from the internet and the lineament map of the image was generated using the necessary filters and thresholds (Figure 5a, 5b).

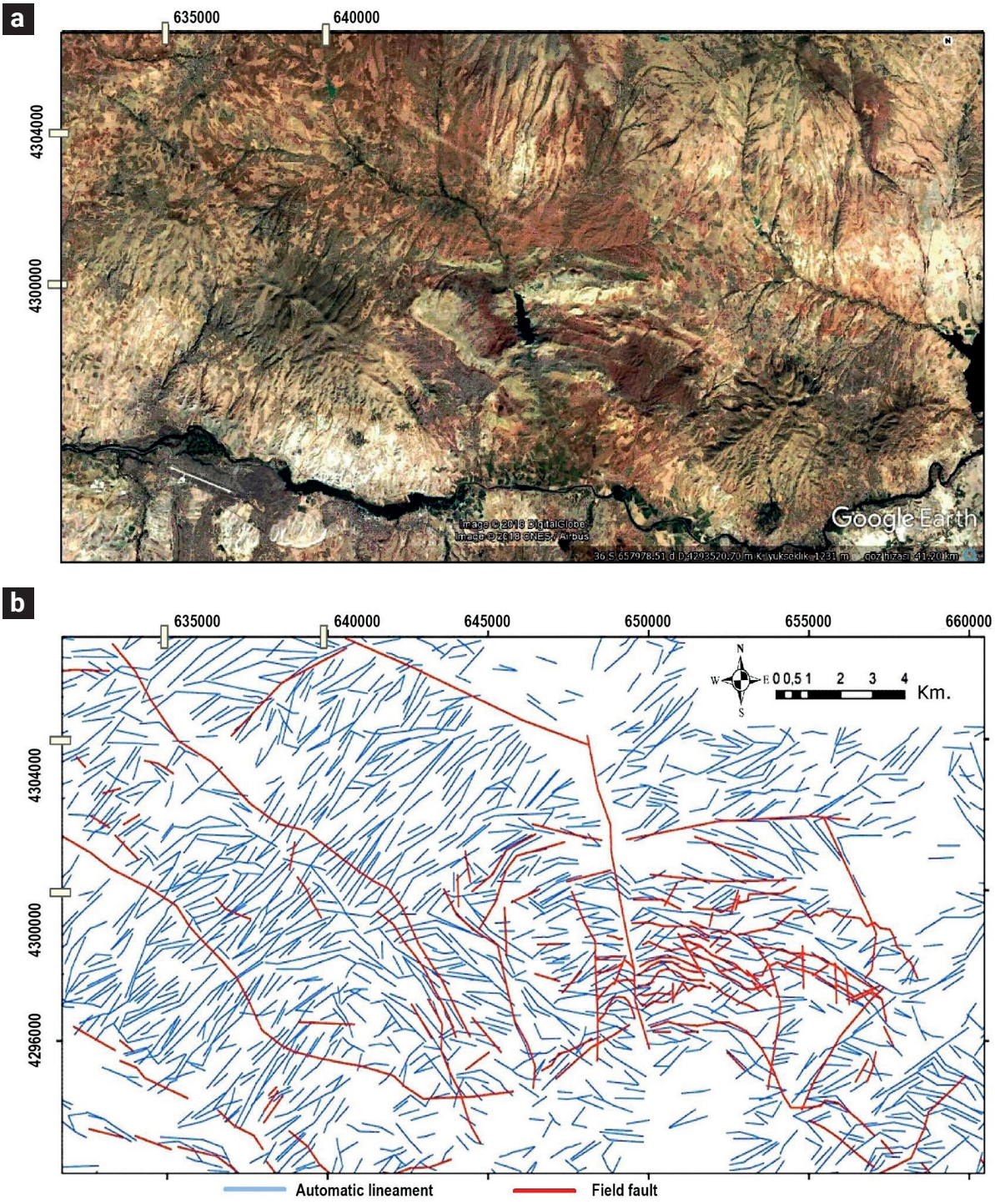

Figure 5. a) Google Earth image of the study area. b) Automatically generated lineament map.

In the generated lineament map, the images were reviewed and lineaments related to artificial structures such as roads, etc. were eliminated. Automated lineaments are predominantly trending N15-30^{0}E and N75-90^{0}W. A certain proportion of the automated lineaments coincided with faults identified in the field (Figure 5b). Another image used to generate automated lineaments is the Landsat 8 satellite image (Figures 6a and 6b).

4.2 Automated lineament maps from satellite image

The Landsat 8 satellite image (Positional resolution between 10-100 metres and spectral resolution ranges from 0.45 to 0.52 µm.) was downloaded from the relevant website (Explorer, 2018) and the image of the area was selected and adjusted using GIS methods. The picture was processed using the filters and

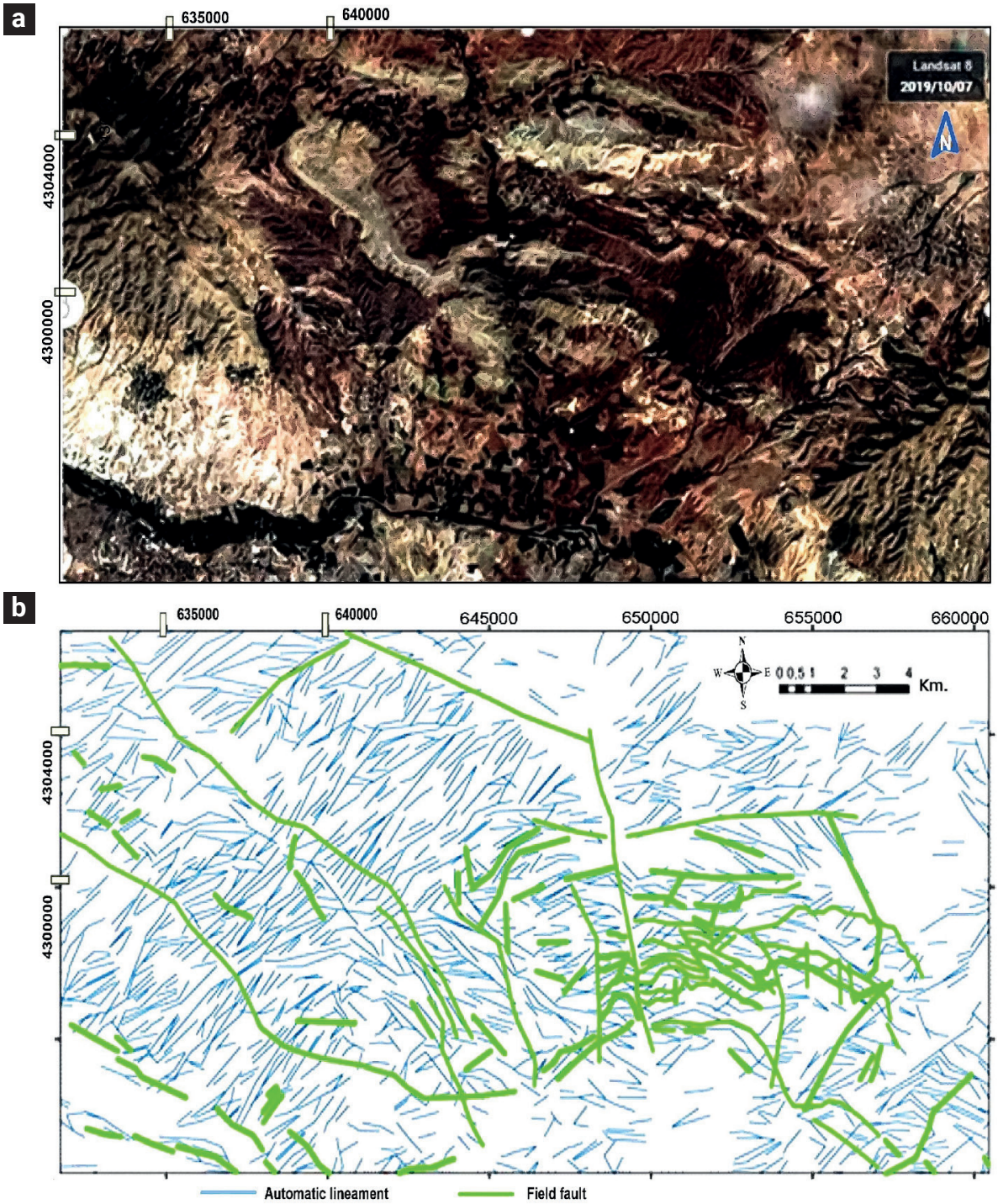

Figure 6. a) Landsat-ETM 8 satellite image of the study area and its surroundings. b) Automatically generated lineament map.

thresholds above to generate an automated lineament map. Again, an attempt was made to eliminate the artificial lineaments by comparing the image and the lineament map.

When the generated lineament map was examined, it was found that the lineaments were generally compatible with the main N-S and NW-SE trending faults identified in the field. However, some of the faults in the study area do not coincide with the lineament map (Figures 6 a, b).

Digital Elevation Model (DEM) imagery is another image used in the automatic generation of the lineament map of the study area. Topographic maps at a 1:25,000 scale were used to generate the DEM images (Figures 7a, b).

The map was digitised at 10m contour intervals. A DEM image with a resolution of 10×10 meters was generated from the digitized elevation values using a suitable GIS program (Figure 7b).

A Shaded Relief Map (SRM) was generated from the DEM image using different illumination directions and a 45° illumination gradient (Figure 8).

Hillshade/shaded relief maps belonging to 8 different viewing directions such as 0°, 45°, 90°, 135°, 180°, 225°, 270°, and 315° were generated (Figure 9).

Integrated shaded relief maps were produced from these maps using appropriate GIS merging techniques. Integrated shaded relief maps covering east (0°, 45°, 90°, 135°) and west (180°, 225°, 270°, and 315°) and all viewing directions (0°-315°) were used for automatic lineament mapping (Figures 10 and 11).

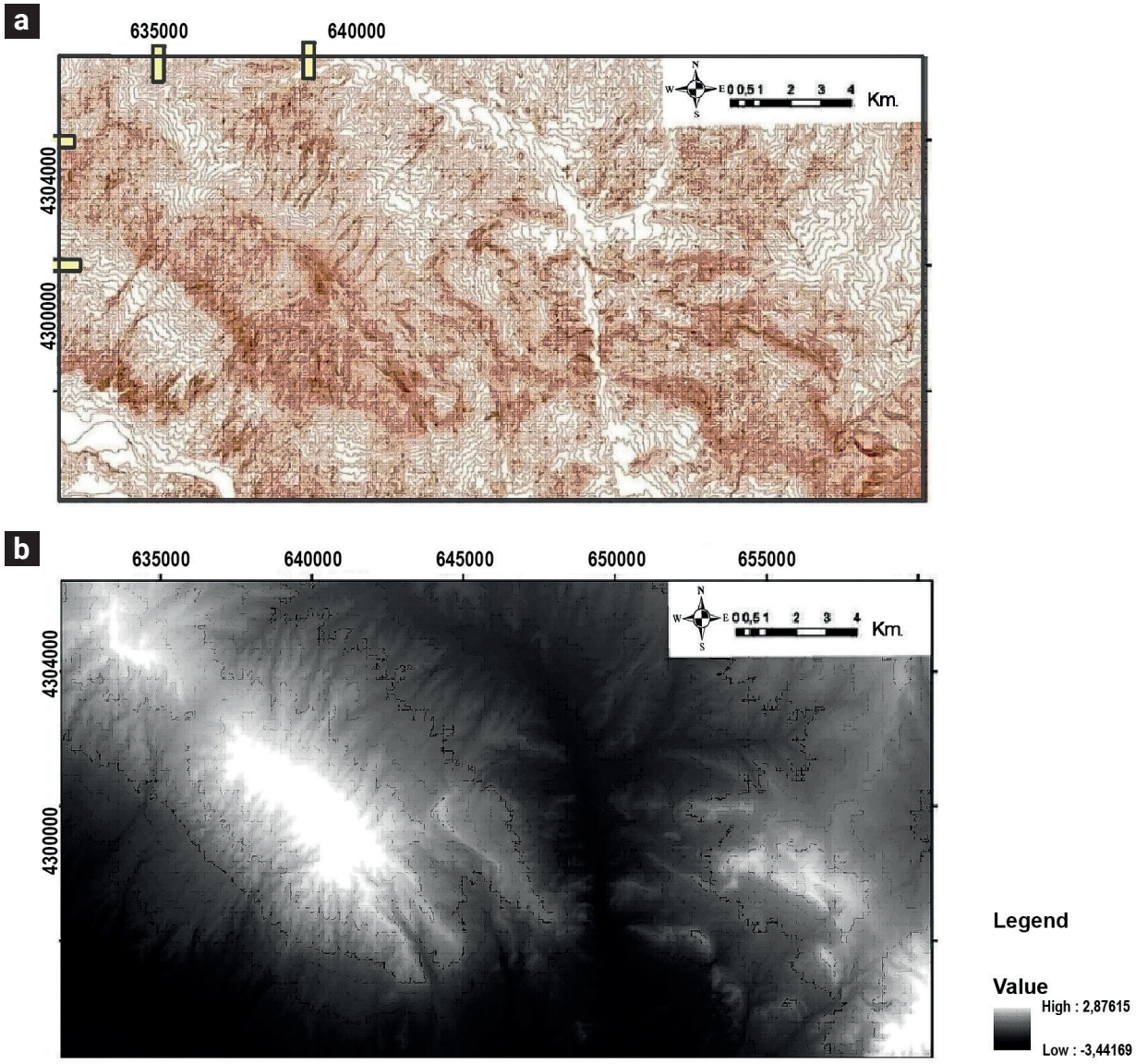

Figure 7. Contour (a) and DEM map (b) were used to derive the Hillshade and Slope Map.

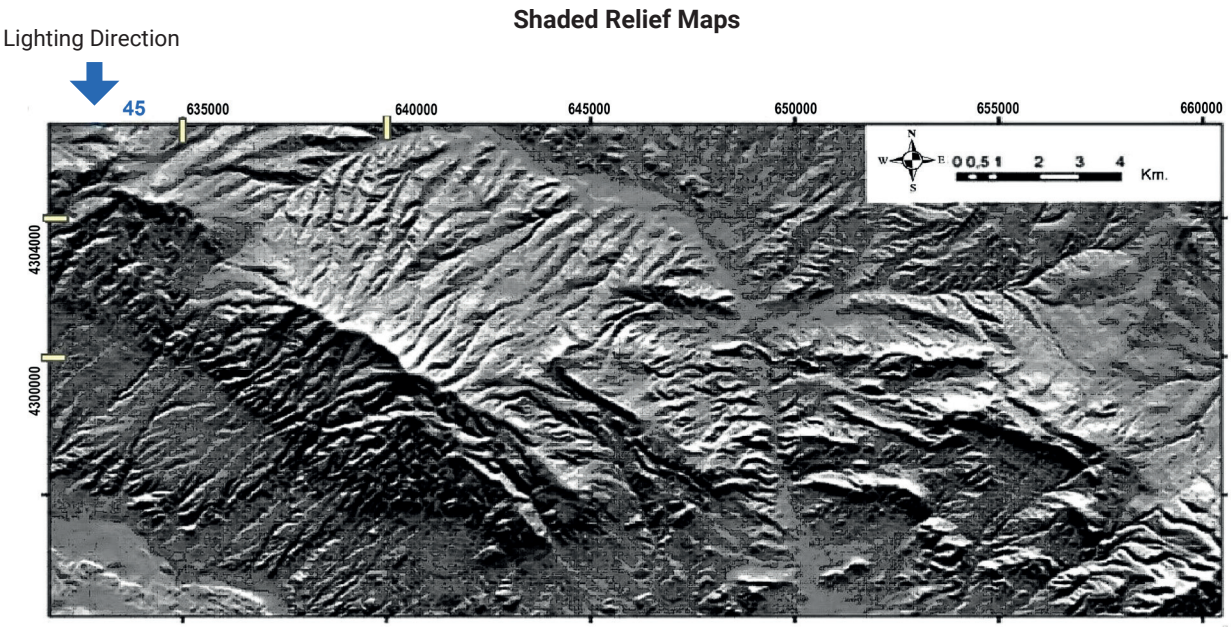

Figure 8. Shaded relief map created from DEM image.

Examination of the lineament maps of the integrated shaded relief maps in the west and east directions shows that these lineaments do not largely represent the faults identified in the study area. North-south and northwest-southeast trending lineaments are dominant on both maps. The automatically extracted lineaments generally do not coincide with the NNE and E-W trending faults in the study area. The lineaments obtained from the integrated shaded relief maps show a more intense distribution than those obtained from the satellite imagery. One of the main reasons for this is the higher resolution of these maps. Again, the lineament maps obtained from the integrated shaded relief maps reveal a fairly dense distribution compared to the faults observed in the field, as well as a homogenous distribution throughout virtually the whole area, except the eastern section, which has rather flat terrain.

One explanation for this is that the faults found in the field typically occur at various formation boundaries. Intra-formation faults are more difficult to detect and map.

Second, formation boundaries and stratification in sedimentary rocks can also create lineaments. Since DEM does not include linear trending structures such as man-made roads, etc., it has an advantage in producing maps containing lineaments of geological origin. The lineaments derived from the integrated shaded relief maps covering all viewing directions show more overlap with the faults in the study area than those derived from other maps (Figure 10). The profile curvature map (Figure 12) and the dip map (Figure 13) were also used to generate lineament maps.

These maps were produced from 10×10 meter resolution DEM images using appropriate GIS methods. To derive the lineament map from these generated maps, the filters were applied similarly to other images and predefined thresholds were used. The lineament map derived from the profile curvature map (Figure 11) is concentrated in the WNW-ESE and NNE-SSW directions, representing the orientation of the faults in the study area. However, it did not generally coincide with the faults identified in the field.

According to the dip map, the eastern part of the study area is horizontal or nearly horizontal, while the dip of the western parts varies between 100-3500 (Figure 13). The lineament map derived from the slope gradient map shows the best agreement with the field faults in terms of strike (Figure 13).

Similarly, the lineaments derived from the slope gradient map overlap the faults the most (Figure 14).

Another method used to compare faults mapped in the field and automatically generated lineament maps is to compare their orientations. For this reason, strike and strike-length rose diagrams were constructed from the lineaments derived from satellite imagery and DEM maps (Figures 15 and 16). The rose diagrams of the faults show an NW-SE and NE-SW trend (Figure 15a). When the lineaments of fractures and faults are evaluated together, they give NW-SE and NE-SW trends (Figure 15b, c). When the field lineaments are evaluated together, they give a dominant NW-SE trend (Figure 15d). It can be seen that the most compatible diagrams are those obtained from the field data (Figures 15 a, b, c, d). The rose diagram is obtained from the shaded relief map (Figure 15 e). There is less agreement with the rose diagrams obtained from the slope and profile curvature map (Figure 15 f, g).

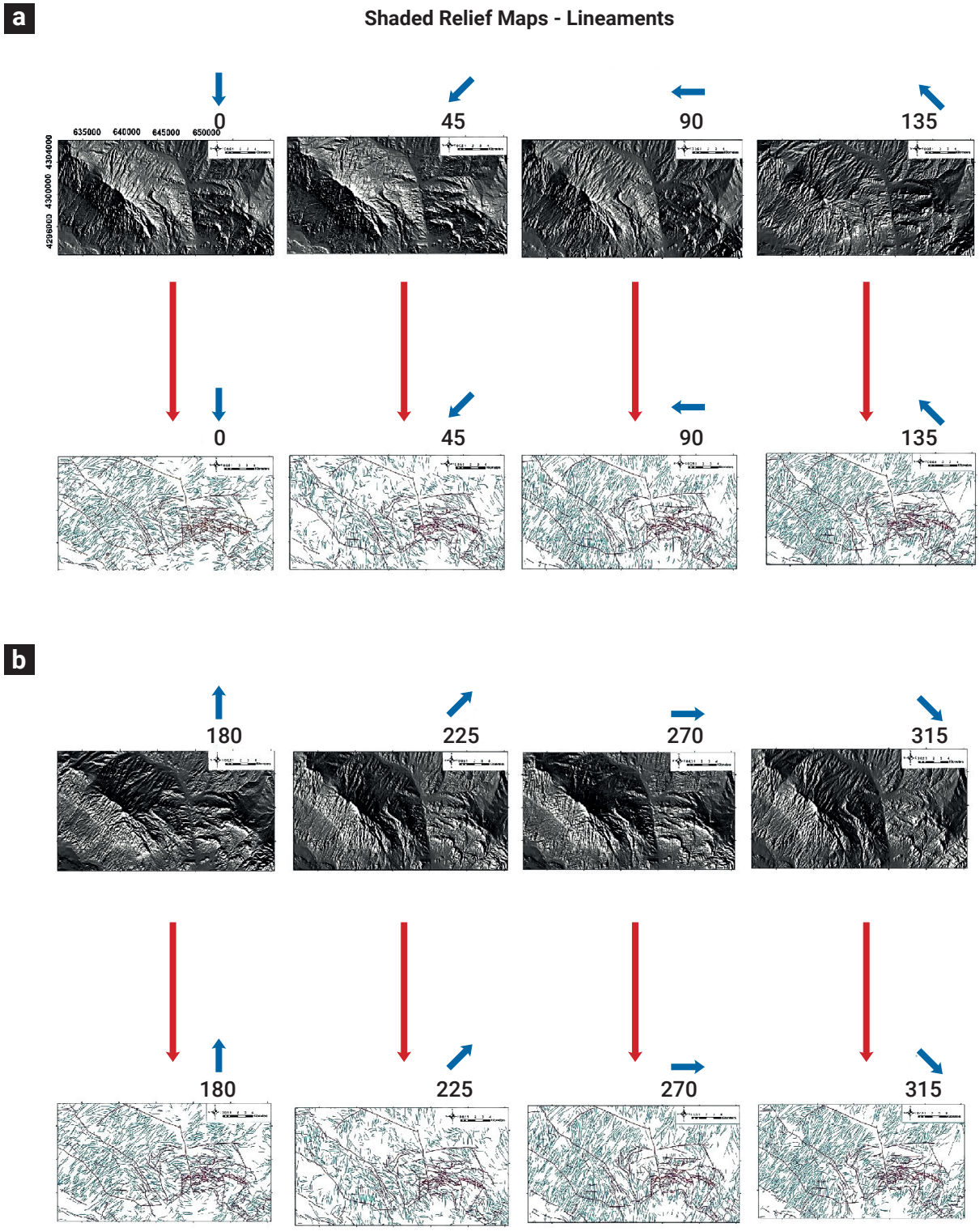

Figure 9. a) Shaded relief maps and lineaments of 0°, 45°, 90°, and 135° viewing directions of the study area. b) Shaded relief maps and lineaments of the 180°, 225°, 270° and 315° viewing directions of the study area.

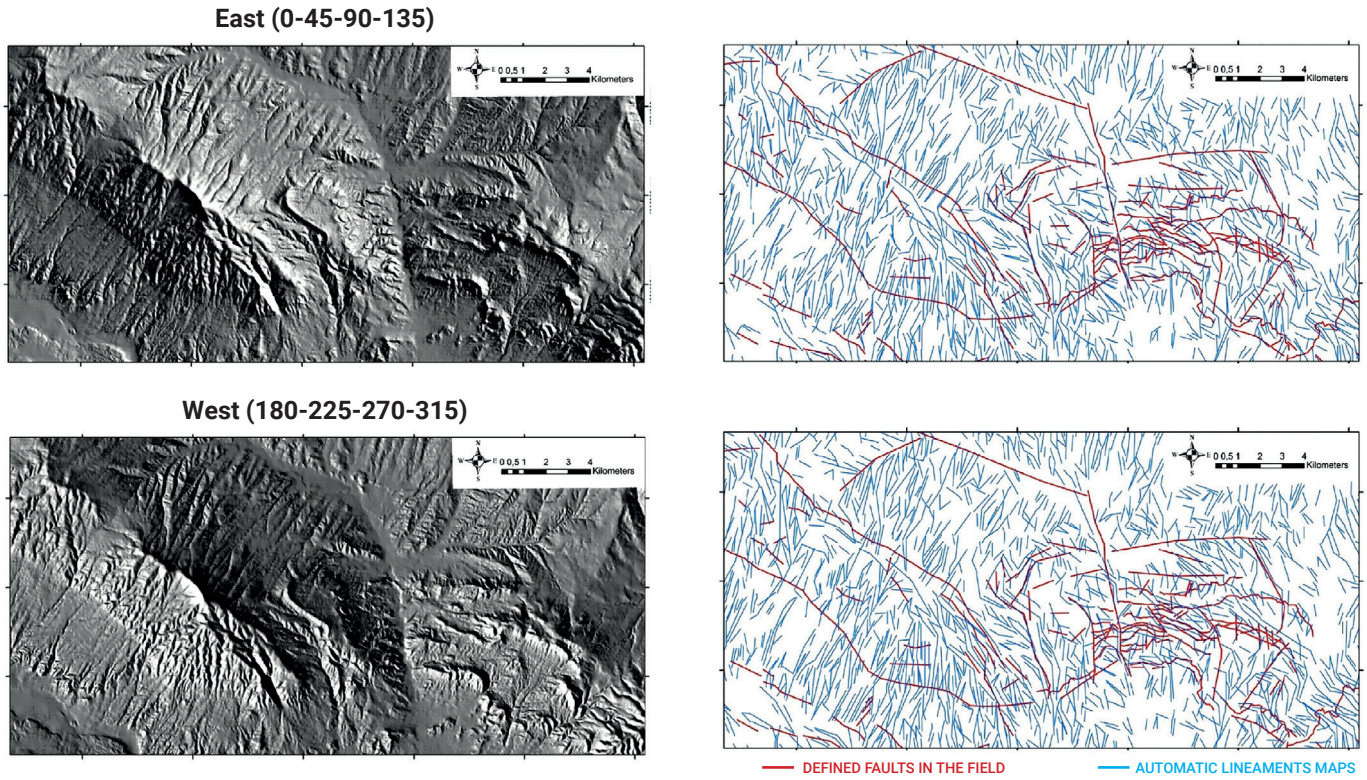

Figure 10. Integrated shaded relief maps of the study area for West (180°, 225°, 270°, and 315°) and East (0°, 45°, 90°, 135°) and their automated lineament maps.

Integrated Shaded Relief Maps (ISRM) and Lineaments

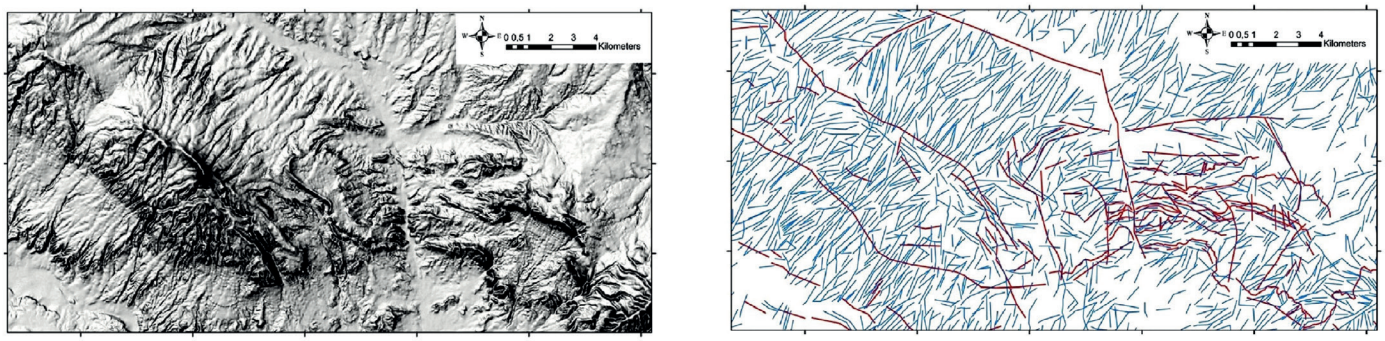

Figure 11. Integrated shaded relief map and linearity of the study area for all viewing directions (0°,45°, 90°, 135°, 180°, 225°, 270°, 360°).

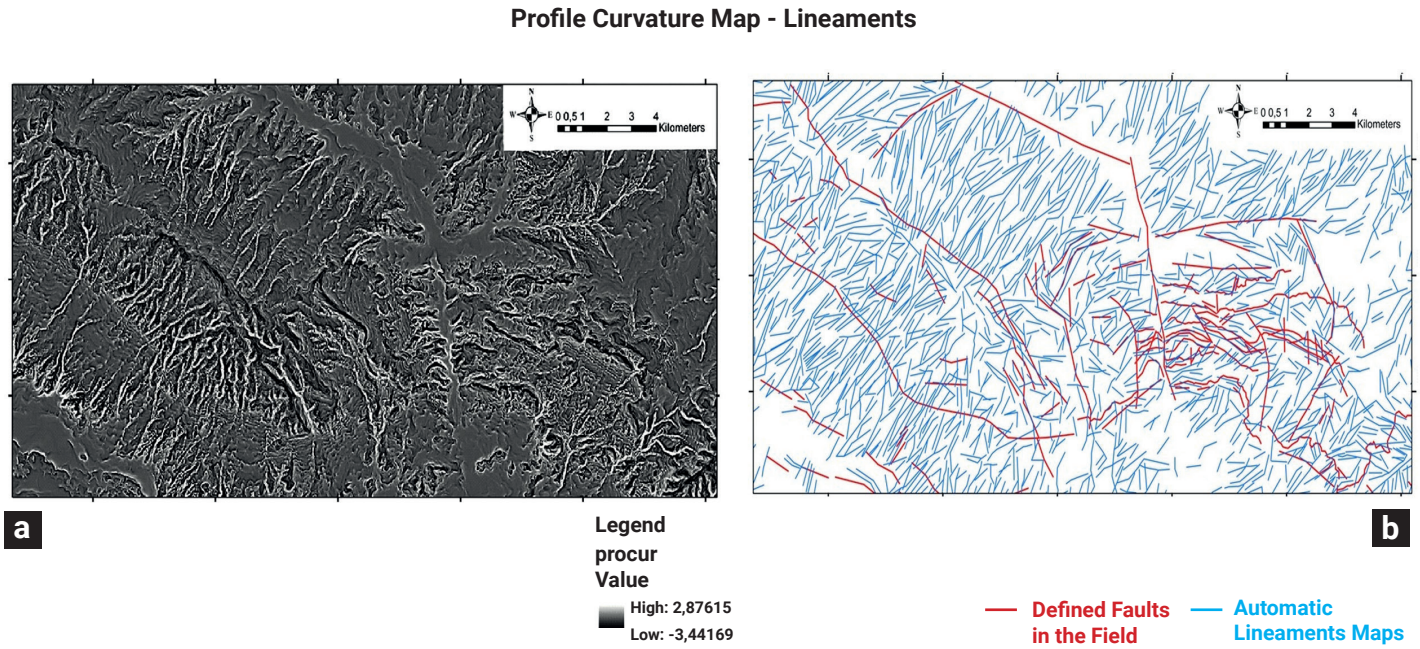

Figure 12. a) Profile curvature map of the study area and b) related lineaments.

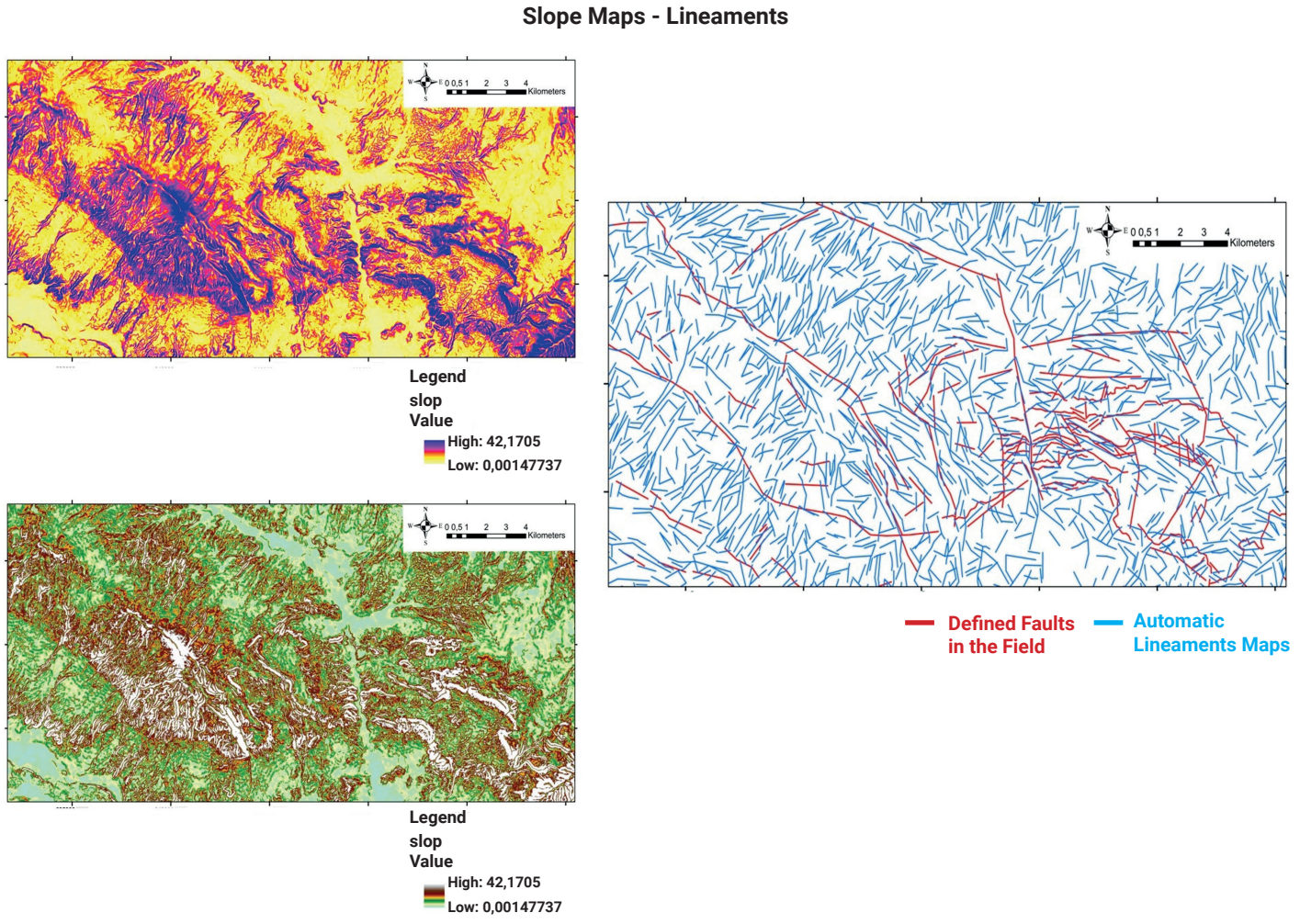

Figure 13. Slope map of the study area and related lineaments.

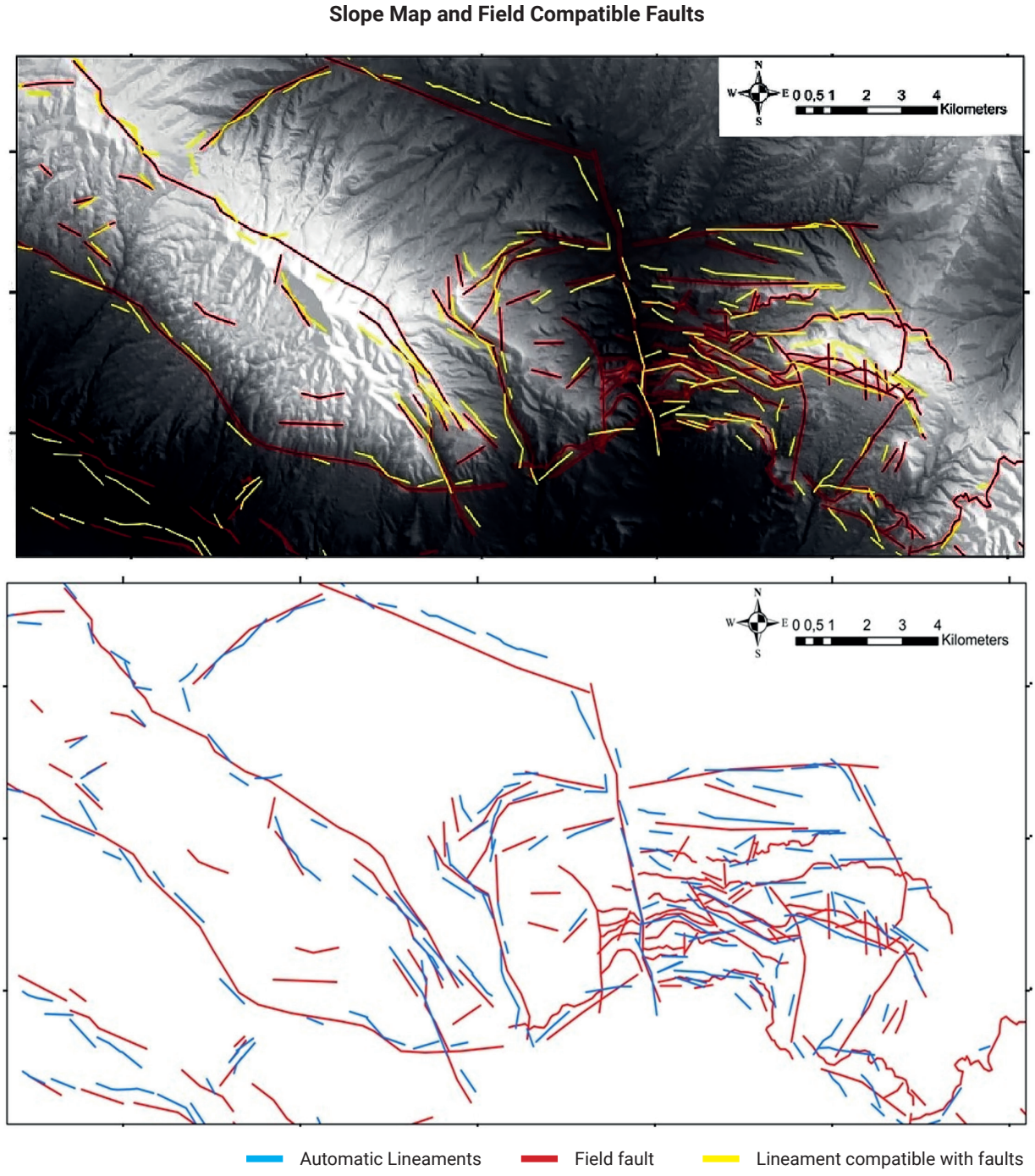

Figure 14. Slope map and field-compatible faults.

The lineaments obtained from the east and west-shaded relief maps of the Landsat ETM-8 satellite images show the dominant lineaments. It can be seen that the most compatible diagrams are those obtained from the field data (Figures 16 a, b, c, d). Some of which are NNE-SSW trending (Figures 16 e, g, h, j, l, m). Some of them are approximately N-S and NW-SE (Figures 16 f, k).

Rose diagrams of lineaments obtained from Landsat-8 and Google Earth images were also generated (Figures 17a, b). In general, similar lineament trends were obtained. In these rose diagrams, lineaments developed in all directions. Dominant lineaments orientations, N0-100E, N40-500E, N70-800E, and N50-600W, N70-800W and N80-900W.

The general trends of the lineaments obtained from satellite images are consistent with the lineaments obtained from the terrain, shaded relief, and slope maps.

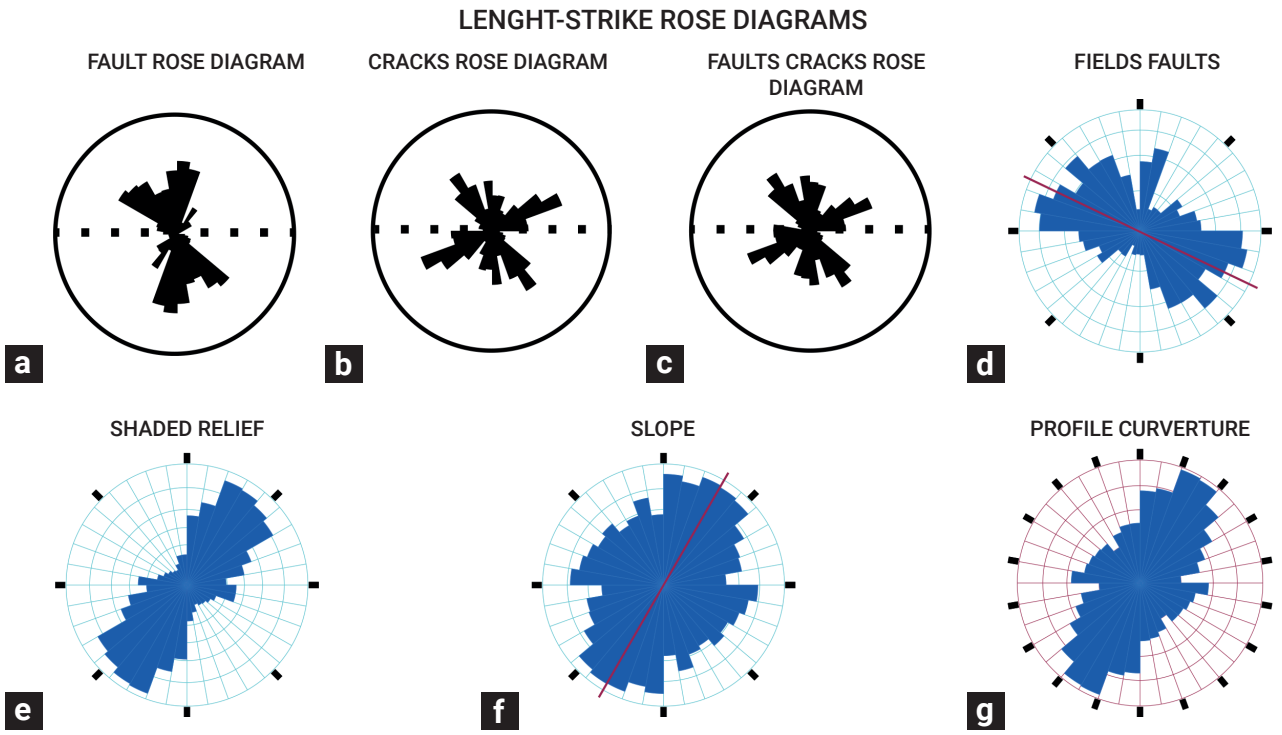

Figure 15. Automated lineament maps and rose diagrams of the strikes of faults.

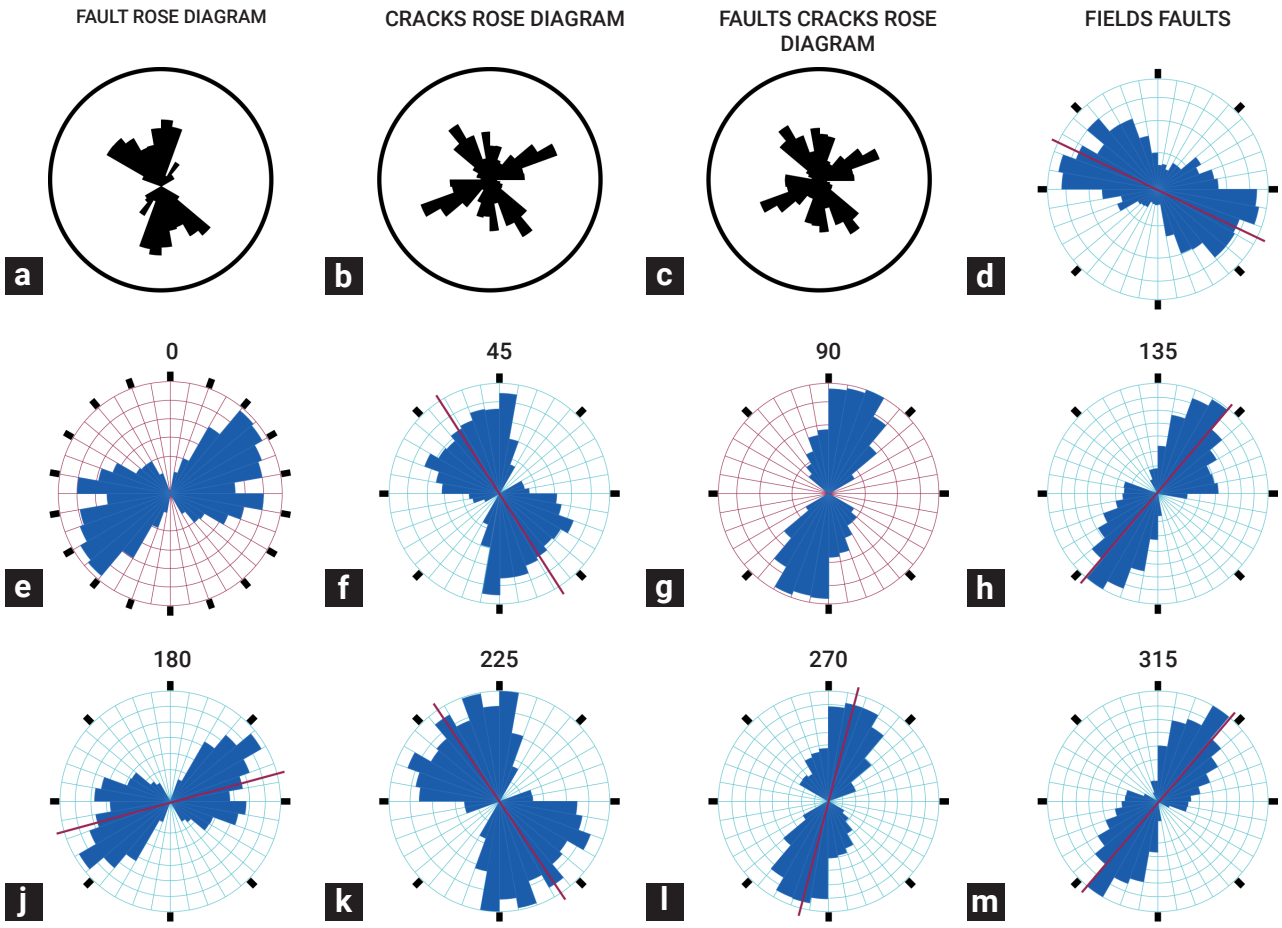

Figure 16. Rose diagrams of lineaments obtained from field data and shaded relief map.

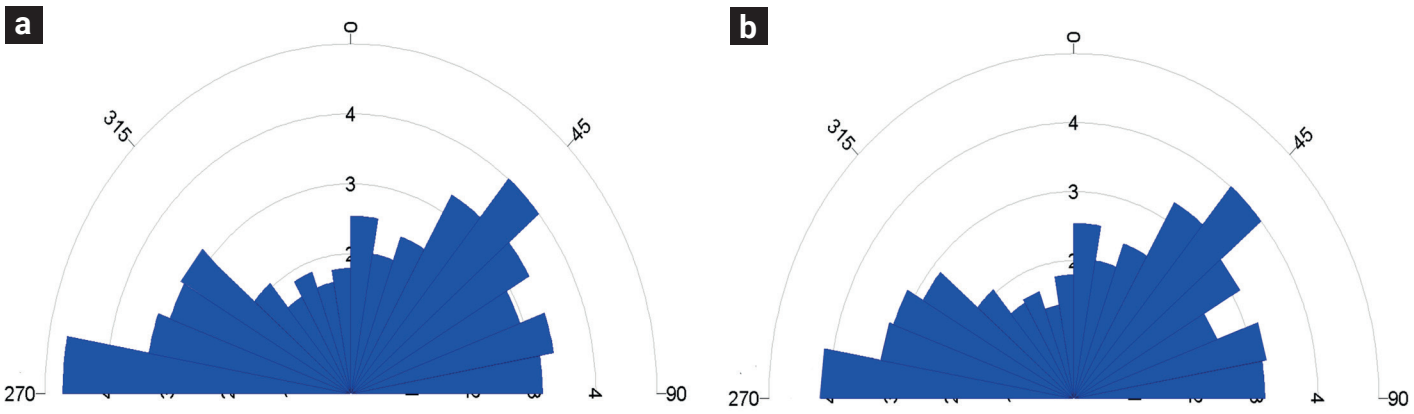

Figure 17. a) Landsat image-based lineament rose diagram. b) Google Earth image-based lineament rose diagram

5. Conclusion and discussion

Lineaments of faults and fractures detected by field observations of the study area were compared with the lineaments obtained from satellite images (Landsat-8 and Google Earth) and computerised topographic maps, slope gradient maps, integrated hillshade maps, and profile curvature maps. It is seen that the orientations of the lineaments obtained from these maps are compatible with the faults and fractures detected in the field in the rose diagrams prepared.

The lineament map obtained from the slope maps is compatible with the majority of the faults and fractures identified in the field.

Fault and fracture orientations developed during the polyphase deformation in the study area vary. Natural and artificial structures such as valleys, valley sides, and artificial boundaries, which are not related to faults and fractures, also show lineaments in satellite images (Google Earth and Lansat 8). These are not included in the evaluation. In this study, similarities are observed between the automatically generated lineaments from fieldwork observations and satellite images.

The general orientation of the lineaments obtained from the Shaded Relief Maps was determined as N20-500E.

The orientations of the lineaments obtained from the slope maps are in good agreement with the lineaments obtained from satellite images (Landsat-8 and Google Earth) and field studies. According to the slope maps, the orientation of the lineaments was determined as N0-100E, N30-500E, N20-300W, N40-500W, and N80-900W.

In the rose diagrams of the lineaments obtained from Landsat-8 and Google Earth images, the orientations of the lineaments were determined as N0-100E, N40-500E, N70-800E, and N50-600W, N70-800W and N80-900W.

Lineaments extracted from Hillshade maps show less homogeneity in areas where the topography is flat. These lineaments appear to be less compatible with faults and fractures in the terrain.

The profile curvature map was used for experimental purposes. However, it was determined that the lineaments obtained from this map are generally unrelated to the faults identified in the field.

In this study, the lineaments obtained by remote sensing are in agreement with the lineaments obtained by fieldwork studies. However, it has been shown that they should be supported by fieldwork observations. The revealed lineaments contribute to the tectonic interpretation of the region. The lineaments detected in the region will contribute to the exploration of water resources and mineral deposits.

6. Author contributions

The authors declare that they contributed to the paper in an equal way.

7. Declaration of competing interest

The authors declare that they have no known competing financial interests or personal relationships that could have appeared to influence the work reported in this paper.

8. Data availability

Data will be made available on request.

9. Acknowledgements

As authors, we would like to thank the editors and reviewers for their efforts and interest.

10. References

Abdelouhed, F., *et al.* (2022). Extraction and analysis of geological lineaments by combining ASTER-GDEM and Landsat 8 image data in the central high atlas of Morocco. *Natural Hazards, 111*(2), 1907-1929. doi: **https://doi.org/10.1007/s11069-021-05122-9**

Abdullah, A., Akhir, J. M. and Abdullah, I. (2010). The extraction of lineaments using slope image derived from digital elevation model: A case study of Sungai Lembing-Maran area, Malaysia. *Journal of Applied Sciences Research*, 6(11), 1745-1751.

Abdullah, S. N. and Abdoh Ghaleeb, A. (2013). Landsat ETM-7 for lineament mapping using automatic extraction technique in the SW part of Taiz Area, Yemen. *Global Journal of Human-Social Science Research*, 13(3).

Abebrese, S., *et al.* (2022). Assessment of groundwater potential zones using GIS and remote sensing techniques in the Bole District, Savannah Region, Ghana. *International Journal of Energy and Water Resources*, 6(4), 445-456. doi: **https://doi.org/10.1016/j.ejrh.2022.101197**

Abu El-Magd, S.A. and Embaby, A. (2021). To investigate groundwater potentiality, a GIS-based model was integrated with remote sensing data in the Northwest Gulf of Suez (Egypt). *Arabian Journal of Geosciences*, 14 (24), 1-12. doi: **https://doi.org/10.1007/s12517-021-08396-2**

Ahmadi, H., Pekkan, E., Seyitoğlu, G. (2023). Automatic lineaments detection using radar and optical data with an emphasis on geologic and tectonic implications: a case study of Kabul Block, eastern Afghanistan. Geocarto International, 38:1. doi: **https://doi.org/10.1080/10106049.2023.2231400**

Altafi Dadgar, M., *et al.* (2017). Extracting of prospective groundwater potential zones using remote sensing data, GIS, and a probabilistic approach in the Bojnourd basin, NE of Iran. *Arabian Journal of Geosciences, 10*(5), 1-11. doi: **https://doi.org/10.1007/s11069-021-05122-9**

Arenas Abarca, M. A. (2006). Lineament extraction from digital terrain models: case study San Antonio del Sur area, south-eastern Cuba. [Master's Thesis] Institute for Geo-information Science and Earth Observation.

Atabey, E., *et al.* (1988). Hacıbektaş, Gülşehir, Kalaba (Nevşehir)Himmetdede (Kayseri) arasının jeolojisi, *M.T.A. Rapor No: 8523, Ankara.* (yayımlanamamış).

Begg, J. and Mouslopoulou, V. (2010). Analysis of late Holocene faulting within an active rift using lidar, Taupo Rift, New Zealand. *Journal of Volcanology and Geothermal Research*, 190 152-167. doi: **https://doi.org/10.1016/j.jvolgeores.2009.06.001**

Bhuiyan, C. (2015). Hydrological characterization of geological lineaments: a case study from the Aravalli terrain, India. *Hydrogeology Journal, 23*(4), 673-686. doi: **https://doi.org/10.1007/s10040-015-1239-0**

Bruning, J., Gierke, J., Maclean, A. (2011). An Approach to Lineament Analysis for Groundwater Exploration in Nicaragua. *Photogrammetric Engineering & Remote Sensing,* 77(5), 1-11. doi: **https://doi.org/10.14358/PERS.77.5.509**

Cracknell, A.P., and Hayes, L.W.B. (1993). Introduction to Remote Sensing. Taylor and Francis, London.

Demircioğlu, R. (2014). Gülşehir-Özkonak (Nevşehir) çevresinde Kırşehir masifi ve örtü birimlerinin jeolojisi ve yapısal özellikleri, Selçuk [Doktora tezi Konya, Üniversitesi Fen Bilimleri Enstitüsü,Yayımlanmış]. Selcuk University Digital Archive SystemsDSpace. **http://acikerisimarsiv.selcuk.edu.tr:8080/xmlui/**

Dirik, K. and Göncüoglu, M.C. (1996). Neotectonic characteristics of central Anatolia. *International Geology Review*, 38(9), 807-817. doi: **https://doi.org/10.1080/00206819709465363**

Drury, S.A., and Walker, A.S.D. (1987). Display and enhancement of gridded aeromagnetic data of the Solway Basin. *International Journal of Remote Sensing*, 8(10), 1433-1444. doi: **https://doi.org/10.1080/01431168708954787**

Eren Y. (2003). Konya Bölgesinin Depremselliği. *Türkiye Petrol Jeologları Derneği Bülteni*, 5, 85-98.

U.S. Geological Survey (02 de abril 2024) Earth Explorer. **http://edcsns17.cr.usgs.gov/** NewEarthExplorer, 122.

Ganguly, K. and Mitran, T. (2016). Delineation and assessment of Central Indian Suture through lineament extraction approach using Remote Sensing and Geographic Information System. *Geocarto International*, 31(3), 308-327. doi: **https://doi.org/10.1080/10106049.2015.1047417**

Goswami, S., Raı, A, and Trıpathy, S. (2022) Re-visiting Geothermal Fluid Circulation, Reservoir Depth and Temperature of Geothermal Springs of India. *Journal of Hydrology*, 412, 123-131. doi: **https://doi.org/10.1016/j.jhydrol.2022.128131**

Göncüoğlu, M. C., Yalınız, M. K., İlkay, K., Köksal, S., & Dirik, R. K. (1993). Orta Anadolu Masifinin orta bölümünün jeolojisi Bolum 3 Orta Kızılırmak Tersiyer Basenininjeolojik evrimi. **https://hdl.handle.net/11511/70566**

Hajaj, S., El Harti, A., Jellouli, A. (2022). Assessment of Hyperspectral, Multispectral, Radar, and Digital Elevation Model data in structural lineaments mapping: A case study from Ameln Valley shear zone, Western Anti-Atlas Morocco. *Remote Sensing Applications: Society and Environment*, 27, 100819. doi: doi.org/10.1016/j.rsase.2022.100819.

Hobbs, B. E., Means, W. D., Williams, P. F. (1976). An outline of structural geology: Wiley.

Hobbs, W. H. (1904). *Lineaments of the Atlantic border region. Bulletin* of the Geological Society of America, 15(1), 483-506. doi: **https://doi.org/10.1130/GSAB-15-483**

Hung, L., Batelaan, O., De Smedt, F. (2005). Lineament Extraction And Analysis, Comparison of Landsat Etm And Aster İmagery. Case Study: Suoimuoi Tropical Karst Catchment, Vietnam. Remote Sensing For Environmental Monitoring, Gıs Applications, And Geology: *Proc. of SPIE* 5983:12. doi: **https://doi.org/10.1117/12.627699**

Isiorho, S.A. (1985). The significance of lineaments mapped from remotely sensed images of the 1:250 000 Lau Sheet in the Benue trough of Nigeria.

International Journal of Remote Sensing, 6(6), 911-918. doi: **https://doi.org/10.1080/01431168508948514**

Işık, A. (1988). Late Paleozoic evolution of the Kütahya-Bolkardağ belt. METU Journal of Pure and Applied Science, 21(1/3), 211-220.

Jacques, P.D., Machado, R., and Nummer, A.R. (2012) Comparison for a multiscale study of structural lineaments in southern Brazil: LANDSAT-7 ETM+ and shaded relief images from SRTM3-DEM. *Anais da Academia Brasileira de Ciências*, 84(4), 931-942. doi: **https://doi.org/10.1590/S0001-37652012000400008**

Jordan, G. and Schott, B. (2005). Application of wavelet analysis to the study of the spatial pattern of morphotectonic lineaments in digital terrain models, A case study. *Remote Sensing Environment*, 94(1), 31–38. doi: **https://doi.org/10.1016/j.rse.2004.08.013**

Keppel, M.N., Karlstrom, K., Crossey, L., Love, A.J., and Prıestley, S. (2020). Evidence for intra-plate seismicity from spring-carbonate mound springs in the Kati Thanda–Lake Eyre region, S. Australia: implications for groundwater discharge from the G. Artesian Basin. *Hydrogeology Journal*, 28(1), 297-311. doi: **https://doi.org/10.1007/s10040-019-02049-1**

Koçyiğit, A. (2003). Orta Anadolu'nun genel neotektonik özellikleri ve depremselliği. *Türkiye Petrol Jeologları Derneği Bülteni*, Özel Sayı, 5, 1-26.

Koçyiğit, A. and Doğan, U. (2016). The strike-slip neotectonic regime and related structures in the Cappadocia region: a case study in the Salanda basin, Central Anatolia, Turkey. *Turkish Journal of Earth Sciences*, 25(5), 393-417. doi: **https://doi.org/10.3906/yer-1512-9**

Koçyiğit, A. (1984). Güneybatı Türkiye ve yakın dolayında levha içi yeni tektonik gelişim. *Türkiye Jeoloji Kurumu Bülteni*, 27(1), 1-16.

Kresic, N. (1995). Remote Sensing of Tectonic Fabric Controlling Groundwater Flow in Dinaric Karst. *Remote Sensing of the Environment*, 53(2), 85-90. doi: **https://doi.org/10.1016/0034-4257(95)00042-Y**

Kuşcu, I. (2001). Geochemistry and mineralogy of the skarns in the Celebi district, Kırıkkale, Turkey. *Turkish Journal of Earth Sciences.* 10(3). 121-132. **https://journals.tubitak.gov.tr/earth/vol10/iss3/3**

Lee, T.H. and Moon, W.M. (2002). Lineament Extraction from Landsat TM, JERS-1 SAR, and DEM for Geological Applications. *IEEE*, 6, 3276-3278. doi: **https://doi.org/10.1109/IGARSS.2002.1027154**

Listyani, R.A.T., Sulaksana N., Csssa, B.Y., Sudradjat, A., and Haryanto, A.D. (2018) Lineament control on spring characteristics at central West Progo Hills, Indonesia. *International Journal of GEOMATE*, 14, 177-184. doi: **https://doi.org/10.21660/2018.46.70127**

Madani, A.A. (2001). Selection of the optimum Landsat Thematic Mapper bands for automatic lineaments extraction, Wadi Natash area, southeastern desert, Egypt. Asian Journal of Geoinformatics. 3(1), 71-76.

Masoud, A. and Koike, K. (2006). Tectonic architecture through Landsat-7 ETM+/SRTM DEM-derived lineaments and relationship to the hydrogeologic setting in Siwa region, NW Egypt. *Journal of African Earth Sciences*, 45(4-5), 467-477. doi: **https://doi.org/10.1016/j.jafrearsci.2006.04.005**

Okay, A. I. and Tüysüz, O. (1999). Tethyan sutures of northern Turkey. Geological Society, *London, Special Publications*, 156(1), 475-515. doi: **https://doi.org/10.1144/GSL.SP.1999.156.01.22**

Raharimahefa, T. and Kusky, T.M. (2009). Structural and remote sensing analysis of the Betsimisaraka Suture in northeastern Madagascar. *Gondwana Research,* 15, 14–27. doi: **https://doi.org/10.1016/j.gr.2008.07.004**

Raj, N. J., Prabhakaran, A., Muthukrishnan, A. (2017). Extraction and analysis of geological lineaments of Kolli hills, Tamil Nadu: a study using remote sensing and GIS. *Arabian Journal of Geosciences*, 10(8), 1-16. doi: **https://doi.org/10.1007/s12517-017-2966-4**

Sedrette, S. and Rebaï, N. (2016). Automatic extraction of lineaments from Landsat Etm+ images and their structural interpretation: Case Study in Nefza region (North West of Tunisia). Journal of Research in Environmental and Earth Sciences, 4, 139-145.

Seymen, İ. (1981). Kaman (Kırşehir) dolayında Kırşehir Masifi'nin stratigrafisi ve metamorfizması, *Türkiye Jeol. Kur. Bült,* 24, 101-108.

Suzen, M. and Toprak, V. (1998). Filtering of satellite images in geological lineament analyses: an application to a fault zone in Central Turkey. *International journal of remote sensing*, 19(6), 1101-1114. doi: **https://doi.org/10.1080/014311698215621**

Sheıkh, H.A., Bhat, M.S., Alam, A., Ahsan, S., and Shah, B. (2022). Assessing the groundwater spring potential of Sindh basin in the Kashmir Himalaya. *Arabian Journal of Geosciences*, 15, 1710. doi: **https://doi.org/10.1007/s12517-022-10965-y**

Tagnon, B. O., Assoma, V. T., Mangoua, J. M. O., Douagui, A. G., Kouamé, F. K., Savané, I. (2020). Contribution of SAR/RADARSAT-1 and ASAR/ENVISAT images to geological structural mapping and assessment of lineaments density in the Divo-Oume area (Côte d'Ivoire). *The Egyptian Journal of Remote Sensing and Space Science*, 23(2), 231-241. doi: **https://doi.org/10.1016/j.ejrs.2018.12.001**

Takorabt, M., Toubal, A.C., Haddoum, H., and Zerrouk, S. (2018). Determining the role of lineaments in underground hydrodynamics using Landsat 7 ETM+ data, case of the Chott El Gharbi Basin (western Algeria). *Arabian Journal of Geosciences*, 11(4), 1-19. doi: **https://doi.org/10.1007/s12517-018-3412-y**

Tessema, A., Mengistu, H., Chirenje, E. (2012). The relationship between lineaments and borehole yield in North West Province, South Africa: results from geophysical studies. *Hydrogeology Journal, 20*(2), 351-368. doi: **https://doi.org/10.1007/s10040-011-0803-5**

Vijhani, A., Sinha, V.S., Vıshwakarma, C.A, Sıngh, P., and Sharma, S.K. (2022). Assessment of diminishing discharge of springs in Central Himalayan region, India. *Hydrological Processes,* 36(5), e14582. doi: **https://doi.org/10.1002/hyp.14582**

Wannous, M., *et al.* (2021). Hydrochemistry and environmental isotopes of spring water and their relation to structure and lithology identified with remote sensing methods in Wadi Araba, Egypt. *Hydrogeology Journal, 29*(6), 2245-2266. doi: **https://doi.org/10.1007/s10040-021-02343-x**

Witt, A. and Carter, M. (2016). Lıdar Lıneament Analysıs of The Central Vırgınıa Seısmıc Zone–Methodology And Prelımınary Results. Geological Society of America Abstracts with Programs, 48(3). Doi: **https://doi.org/10.1130/abs/2016SE-273043**